Composites Science and Technology 154 (2018) 53–63

Contents lists available at ScienceDirect

Composites Science and Technology

journal homepage: http://www.elsevier.com/locate/compscitech

An experimental investigation of the temperature effect on the mechanics of carbon fiber reinforced polymer composites

Zian Jia, Tiantian Li, Fu-pen Chiang, Lifeng Wang*

Department of Mechanical Engineering, State University of New York at Stony Brook, Stony Brook, NY 11794, USA

ARTICLE INFO

Article history:
Received 8 September 2017
Received in revised form
27 October 2017
Accepted 15 November 2017
Available online 16 November 2017

Keywords:
Carbon fiber reinforced polymer composites
Temperature effect
Strain rate effect
Toughening mechanism
Microbuckling
Kinking

ABSTRACT

Carbon fiber reinforced polymer (CFRP) composites are increasingly used in civil, naval, aerospace, and wind energy applications, where they can be frequently exposed to harsh temperature conditions and under static and dynamic loads. The extreme temperature conditions and dynamic loading are critical for CFRP composites structural design as the constituent polymer properties are highly sensitive to temperature and strain rate. This work experimentally investigates the effect of temperature, ranging from −100 °C to 100 °C, on the mechanical properties of CFRP composites under static and dynamic three-point bending tests. The results reveal that CFRP composites provide enhanced flexural strength, maximum deflection, and energy absorption at lower temperatures (−60 °C, −100 °C) while relatively poor performance at a higher temperature (100 °C). Experimental images from the post-mortem photographs, scanning electron microscopy, and high speed videos are implemented to observe various failure behaviors including microbuckling, kinking, and fiber breakage at different temperatures. Analytical modeling is further applied to reveal the underlying mechanisms responsible for these temperature dependent mechanical behaviors. The findings reported here provide insights into the study of the temperature effect on the mechanical response of CFRP composites, which expands the way to design stiffer, stronger and tougher CFRP composites.

1. Introduction

Carbon fiber reinforced polymer (CFRP) composites are widely used in aerospace [1], naval [2], automotive [3], and civil [4] applications due to their high stiffness to weight ratio and high strength to weight ratio. For example, using CFRP instead of metals in automobile vehicles is reported to bring a weight reduction factor as high as 15, significantly improving fuel efficiency, maneuverability, and payload capacity of the vehicles [5]. Compared with traditional materials (e.g. metals), carbon fibers have greater fatigue resistance, better long-term stability, lower thermal expansion and excellent corrosion resistance. Such advantages make CFRP a potential candidate for a wide range of applications in various and extreme environmental conditions [6]. Many efforts have been devoted to the study of CFRP composites under various environmental elements, including moisture [7,8], ultraviolet (UV) radiation [9], and extreme temperatures [10]. Compared with the long-term degradation caused by UV radiation and moisture, which can be resolved by a protective coat together with lifetime monitoring, the temperature changes often happen in a relatively short time and thus can be catastrophic, like the well-known shipwreck of *Titanic* caused by the ductile-brittle transition of steel at a frigid temperature. Similarly, the mechanical properties of the polymer matrix (i.e., modulus, strength, and toughness) are highly temperature dependent [11]: as temperature increases, it transits from a hard glassy state to a soft rubbery state and the modulus can be several orders lower; as temperature decreases, it becomes brittle and cracks propagate easily. Therefore, the mechanical responses of CFRP composites at various temperatures need to be studied carefully such that using them at unfavorable temperatures could be avoided.

Previous investigations on the temperature effect mainly focus on the tensile and compressive experiments of unidirectional CFRP laminates at cryogenic temperatures (−269 °C, −196 °C). These results have been reviewed by Reed [12], showing that the elastic modulus of CFRP increases 10% when cooling to the temperature of −269 °C ~ −196 °C and the tensile strength of CFRP composites increases as well at extremely low temperatures (−196 °C). However, the effect of temperature on the compressive strength of CFRP

* Corresponding author.
E-mail address: lifeng.wang@stonybrook.edu (L. Wang).

https://doi.org/10.1016/j.compscitech.2017.11.015
0266-3538/

remains inconsistent in different studies. A more recent study [13] on the tensile and bending tests of quasi-isotropic and cross-ply laminates at 20 °C, −60 °C and −150 °C indicates that both the strength and the toughness of the CFRP decrease at lower temperatures. Models have also been proposed to correlate composite properties and the temperature for the study of higher temperature effect, assuming that any relaxation in the polymers requires overcoming the constraints of secondary bonds. The matrix shear response [14], heat flux [15], and mass loss [16] in CFRP are important at elevated temperatures.

All these studies have laid a solid foundation to study the temperature effect on the mechanics of CFRP, but there are still challenging issues to be addressed. First, the temperature range, −100 °C–100 °C, has become more important due to recent applications. For example, commercial airplanes (Boeing 777) cruise at 13 km altitude where the ambient temperature is around −60 °C [17]. The temperature range of a low-earth orbit satellite is typically from −170 °C to 120 °C [18]. The lowest and highest temperatures ever measured on the earth ground level are −90 °C in Antarctica [19] and 57 °C in California [20], while a theoretical estimation gives the maximum ground surface temperature in the range of 90 °C–100 °C in extreme conditions [21]. Second, the inconsistency of the reported mechanical properties hinders the utilization of CFRP composites at extreme temperature conditions. The discrepancy may come from many aspects [13,22–24], including the laminate manufacturing (matrix cure level, fiber waviness/alignment) and the differences in testing techniques (grip method and sample size) [25]. Third, the dynamic response of CFRP composites at various temperatures is largely unexplored, considering that vehicles, infrastructures, naval ships, and submarines are particularly susceptible to low velocity impacts. More importantly, the low temperature conditions could further facilitate the initialization and propagation of cracks under dynamic loading.

In this paper, we systematically investigate the temperature effect on the mechanical properties of CFRP composites using static and dynamic three-point bending tests with a temperature range −100 °C–100 °C. The dependency of failure strength, energy absorption, and failure patterns on the temperature is studied. The dynamic effect is highlighted by comparing impacts at different velocities. Finally, the failure mechanisms and the effect of thermal stress are discussed with the aid of theoretical analysis.

2. Experimental methods

High strength carbon fibers (50% volume fraction) reinforced vinyl ester provided by Graphtek LLC is used in this research. The properties of the constituent materials at room temperature are summarized in Table 1. The CFRP specimens are prepared with a dimension of 101.6 mm × 12.7 mm × 1.5 mm and the longitudinal direction of the specimen is cut along the fiber direction (Fig. 1 upper right).

Table 1
Material properties of carbon fiber and vinyl ester matrix at room temperature.

	Carbon Fiber	Vinyl Ester
Modulus, GPa	227	3.5
Tensile strength, MPa	2.8–5.1 × 10^3	70–80
Poisson's ratio	0.3	0.3
Elongation at failure	1.40%	4–6%
Density, g/cm^3	1.8	1.15
Coefficient of thermal expansion α , $\times 10^{-6}$/°C	−4(longitudinal)	16–22

2.1. Static three-point bending test

The static three-point bending tests are performed using a MTS mechanical tester (C43) with a 1 kN load cell following the ASTM d790-10 standard [26]. A MTS Advantage™ environmental chamber (temperature accuracy ±1 °C) is used to enable mechanical tests at various temperatures. Here, the temperatures −100 °C, −60 °C, −20 °C, 25 °C, 60 °C and 100 °C are considered. For each temperature, five specimens are tested and all specimens are kept in the chamber for 20 minutes to achieve homogeneous temperature distribution before the tests. All the experiments are conducted in a quasi-static regime with a constant strain rate of 0.01 (at the out surface of the midspan). The load-displacement curves measured from the three-point bending tests are then transferred into the flexural stress strain behaviors based on the measured dimensions of the specimens. The following equations [26] are adopted to calculate the effective flexural stress σ_f and flexural strain ε_f :

$$\sigma_f = 3PL\Big/2bd^2\Big[1 + 6(D/L)^2 - 4(d/L)(D/L)\Big], \tag{1}$$

$$\varepsilon_f = 6Dd\Big/L^2, \tag{2}$$

where σ_f and ε_f are the stress and strain in the outer surface at midspan, D is the deflection at the center of the beam, P is the load applied at the middle of the span, L is the support span, b and d are the width and depth of beam respectively.

2.2. Dynamic three-point bending test

Dynamic tests are performed using a modified split Hopkinson pressure bar (SHPB) [27,28] system with a liquid nitrogen cooled environmental chamber. Images of the specimens at various loading conditions are taken at a rate of 40000 FPS by a high-speed imaging camera (Photron SA1.1) (Fig. 2). Impact speed is controlled by the pressure of the gas reservoir. The temperature inside the environmental chamber is tuned with liquid nitrogen circulation and monitored with four thermal couples located at separate locations. When the control valve is opened, the high-pressure air accelerates the striker which then transfers its momentum to the impactor that impacts the specimen with the designed dynamic three-point bending condition. The specimens for the dynamic tests are the same as the ones for the static three-point bending tests. The mass of the impactor is 335.26 g and the impact speed (3 m/s to 15 m/s) is achieved by controlling the pressure level. Displacement history and velocity history of the impactor is calculated by digital image correlation (DIC) with commercial software VIC-2D (Correlated Solution Inc.). The energy mitigation capacity of the composites is estimated by kinetic energy loss during the impact

$$E_{dynamic} = KE_{res} - KE_{ini}, \tag{3}$$

where KE_{ini} and KE_{res} are the initial and residual kinetic energy of the impactor. The minimum penetration velocity is also obtained to quantify the penetration resistance of the composite. In addition, the flexural strain rate of the specimen is related to the impact velocity by $\dot{\varepsilon} = 6dv/L^2$ where d is the depth, L is span of the beam, and v is the impact velocity. In our experiments, the relation simplifies to $\dot{\varepsilon} = 2.93v$.

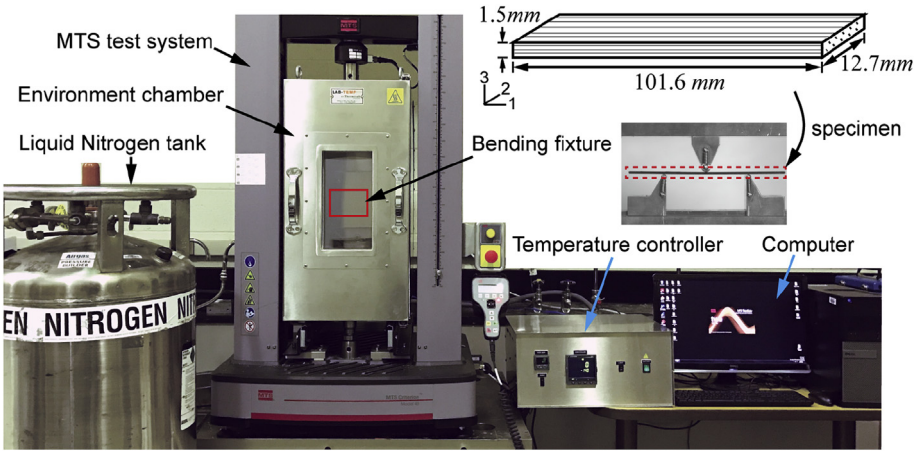

Fig. 1. Static three-point bending test apparatus. A MTS electromechanical material testing system is integrated with an environmental chamber to enable various temperature tests. Liquid nitrogen circulation and a heating module are used for cooling and heating control respectively. The upper right shows the three-point bending fixture and the size of a CFRP specimen.

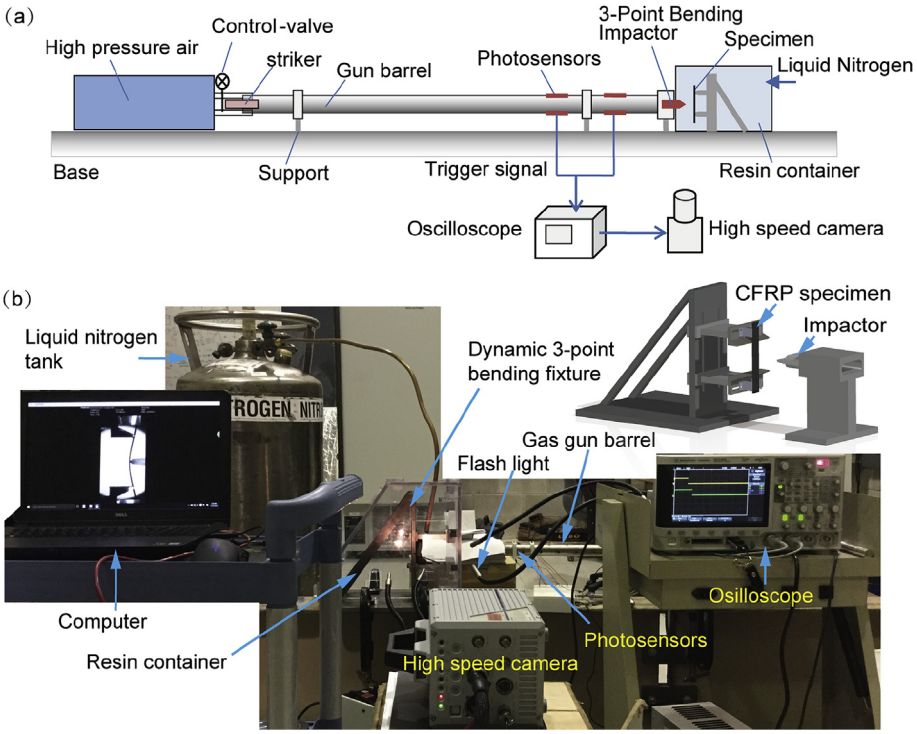

Fig. 2. The modified split Hopkinson pressure bar (SHPB) system for dynamic three-point bending tests. (a) Schematic of the experiment setup, (b) photograph of the SHPB showing the gun barrel, dynamic three-point bending fixture, and the high-speed videoing system.

3. Results

3.1. Static three-point bending results

Fig. 3(a) shows the representative force-displacement curves of the unidirectional CFRP composites under static three-point bending tests at different temperatures. The force-displacement curves for all the specimens exhibit a linear elastic regime followed by a stress drop. The specimens break catastrophically at −60 °C, −20 °C, 25 °C, while at other temperatures the specimens show clear post break strength. In the elastic regime, the flexural modulus of the CFRP composite at 100 °C is about half of those at the other temperatures. For a fully cured vinyl ester, glass transition temperature T_g = 120 °C [29]. At 100 °C, corresponding to normalized temperature $T/T_g = 0.95$ (calculated in K), the matrix is in its glass transition regime and thus rubbery. Large shear deformations (together with small tensile/compressive deformation) mainly take place in the matrix during bending of the CFRP composite. By contrast, the carbon fibers are significantly bended but have relatively small longitudinal deformation (free ends). Thus, the carbon fibers have a relatively low longitudinal stress level, which greatly reduces the flexural modulus of the CFRP composite. On the other hand, when the matrix is in glassy regime ($T < 60$ °C, $T/T_g < 0.85$), the shear stress is transferred effectively, and the elastic

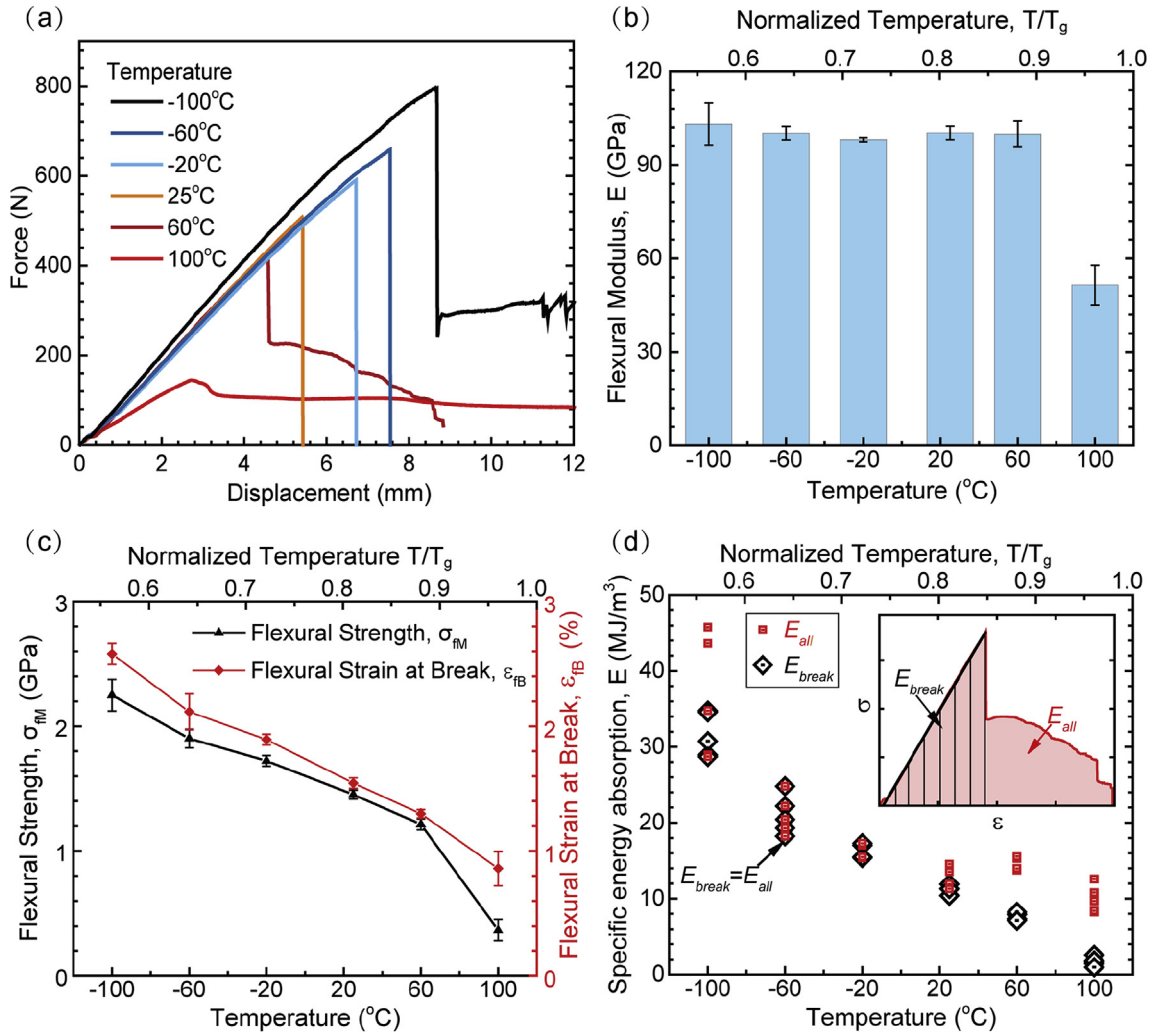

Fig. 3. Static three-point bending results at temperatures from −100 °C to 100 °C. (a) Representative force displacement curves, (b) flexural modulus, (c) flexural strength and flexural strain at break, and (d) specific energy absorption per volume. E_{break} is the energy absorption per volume before specimen break, E_{all} is the overall energy absorption including the part contributed by post break strength, $E_{break} = E_{all}$ indicates no post break strength.

deformation is dominated by carbon fiber tension/compression. As such, the composite's flexural modulus is approaching a constant.

The statistically calculated flexural modulus (E), flexural strength (σ_{fM}), and flexural strain at break (ε_{fB}) are summarized in Fig. 3(b) and (c). Both flexural strength and flexural strain at break increase significantly at lower temperatures. For example, the flexural strength at −100 °C is twice of that at 60 °C, and is 55% higher than that at 25 °C. In addition, the flexural strength and flexural strain have a good linear relationship with temperature ($0.44 < T/T_g < 0.85$), indicating the energy absorption scales with temperature squared.

The energy mitigation capability is evaluated by the energy absorption per volume. The total energy absorption (E_{all}) is set as $E_{all} = E_{break} + E_{post}$ (Fig. 3(d)), where the energy absorption at break (E_{break}) is calculated as the area below the force-displacement curve before break divided by the specimen volume, and the energy absorption at post break (E_{post}) is calculated as the area below the force-displacement curve after break divided by the specimen volume. The specimens at −20 °C and −60 °C exhibit no post-break strength. By contrast, the specimens at −100 °C, 20 °C, 60 °C and 100 °C exhibit significant post-break strength which provides extra energy absorption ability (over 30% at −100 °C). The mechanisms of the post break strength will be explained in the discussion section.

3.2. Damage process and post-mortem sample observation

Fig. 4 shows photographs of the specimens after the static three-point bending tests at different temperatures. The specimen at 100 °C ($T/T_g = 0.95$) exhibits failure at top layers by microbuckling as shown with white arrows in Fig. 4(a). Some matrix fails due to localized deformation, leaving several inter-fiber cracks (yellow arrows). Vinyl ester behaves as an elastomer at this temperature, thus most of the deformation is recovered after unloading, leading to no noticeable plastic deformation. By contrast, shear mode microbuckling is observed at 60 °C, together with noticeable plastic deformation (Fig. 4(b)). At room temperature (25 °C), kink bands first form in the top region of the specimens, followed by inter-fiber cracking in the bottom region of the specimens (yellow arrow in Fig. 4(c)). When the temperature further decreases to −20 °C (Fig. 4(d)) and −60 °C (Fig. 4(e)), the top and bottom regions of the specimens fail simultaneously, and the post-mortem photos show one major crack penetrating through the whole specimen. The major crack is localized in the mid-section perpendicular to the fiber direction. In addition, the upper half crack surface caused by compression shows a neat fracture surface, while the lower half crack surface caused by tension shows a rough zig-zag fracture surface (white arrow in Fig. 4(e)) corresponding to the pulling out

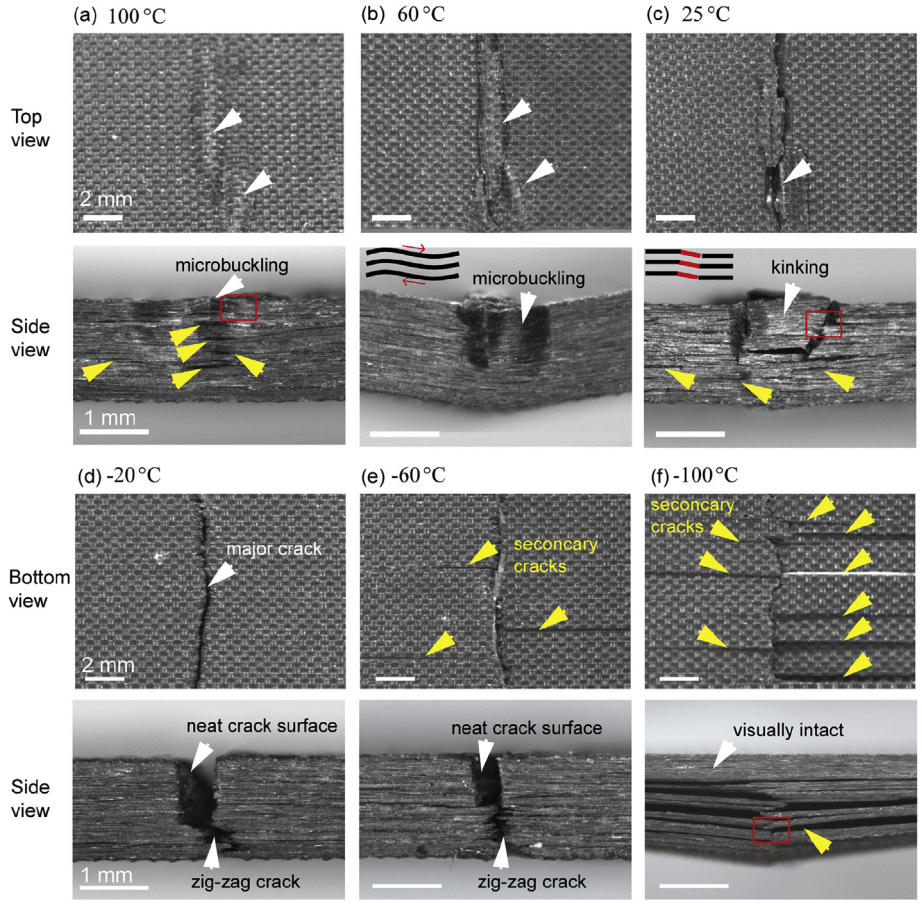

Fig. 4. Post mortem photographs after the static three-point bending tests. (a) Elastic microbuckling, the deformations are mostly recovered after unloading, white arrows show location of buckling and yellow arrows show residual inter-fiber cracks. (b) Shear mode microbuckling. (c) Kink band formation (white arrows) and inter-fiber cracking (yellow arrows). (d) Catastrophic damage with one major crack at −20 °C, with a neat upper fracture surface and a zig-zag bottom fracture surface. (e) One major crack (white arrow) and several secondary cracks (yellow arrows) parallel to the fiber direction. (f) Extensive inter-fiber cracking (yellow arrows) with a brush-like post-damage pattern in the bottom layers, and the upper layers are visually intact. The locations marked by red rectangles are further inspected by SEM in Fig. 5. (For interpretation of the references to colour in this figure legend, the reader is referred to the web version of this article.)

of the carbon fibers under tensile loading. Interestingly, the specimen at −60 °C start to show secondary cracks parallel to the fibers (yellow arrows in Fig. 4(e)). The damage of the specimen at −100 °C is characterized by fiber breakage, which initiates from the lowest surface and gradually propagates upward (Fig. 4(f)). The upper layers stay visually intact, and the damage is delocalized by many secondary cracks parallel to the fiber direction. Inter-fiber cracking is prominent at −100 °C and the failure is characterized by the splitting and fraying of the fiber bundles, leaving a brush-like shape [30] of the post-mortem specimen.

Regions marked with red rectangles in Fig. 4 (at 100 °C, 25 °C and −100 °C) are further inspected by a scanning electron microscope (SEM). Fig. 5(a) shows the original microstructure of the CFRP composite before tests, where ideal fiber-matrix bonding is observed. In Fig. 5(b), the mortem specimen at 25 °C shows the kink bands near the indenter and an enlarged photo (Fig. 5(c)) shows that multiple kink bands are formed, corresponding to the so called "complementary kinking" [31]. Note that the multiple kink bands are formed for the existence of the indenter. Further enlarged views in Fig. 5(d) show the fiber bundles crack normal to the buckling direction, and extensive fiber-matrix debonding is observed. The microscopic deformation at 100 °C is shown in Fig. 5(e) and (f), where most carbon fibers stay intact and fiber rotations (rotation angle ~10°) are observed, suggesting local plastic deformation of the matrix. Moreover, minor inter-fiber cracks are also observed, indicating matrix failure. The damage of the specimens at −100 °C is characterized by a large cracking area with extensive fiber break and zig-zag cracking paths. The fracture surface of the fibers is populated with rows of cusps along the fiber direction, which is similar to that observed in a CFRP fatigue test for very brittle matrix [32].

3.3. Dynamic three-point bending results

Fig. 6 shows the dynamic bending results with an impact velocity v_{ini} ~5 m/s at −100 °C, −60 °C, −20 °C, and 25 °C timing from the moment of impactor-specimen contact. The displacement history in Fig. 6(a) shows the displacement at breakage increases as decreasing the temperature (so is the stress level at failure). It is worth noting that the specimens do not break at −100 °C with the impact velocity of 5 m/s, at which the impactor is bounced back with a velocity around −5 m/s (the whole history is shown in the inset). For this reason, the impact history of $v_{ini} = 6$ m/s at −100 °C is also shown for comparison. The difference in the slop of displacement curves corresponds to the discrepancy in the initial velocities. By contrast, the velocity fluctuation in Fig. 6(b) comes from the numerical error in DIC calculation. Nevertheless, consistent trends are observed that the deflection at break and the time when specimens break increase at lower temperatures. As a result, CFRP composites at lower temperatures are found tougher with

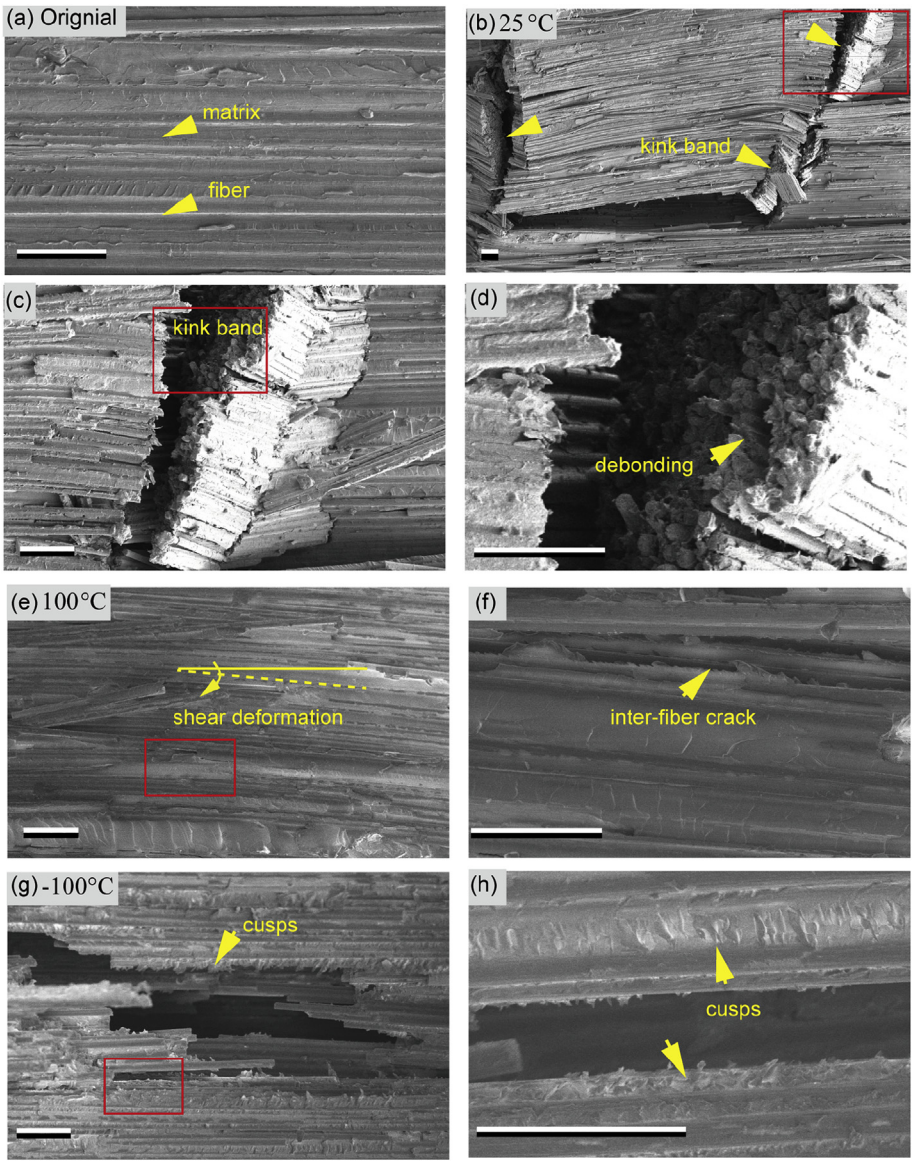

Fig. 5. SEM observation of the (a) original specimen, and post-mortem specimens at (b) (c) (d) 25 °C, (e) (f) 100 °C, and (g) (h) −100 °C corresponding to the regions marked by red rectangles in Fig. 4. (c), (d), and (f), (h) the enlarged regions in (b), (c), (e), (g) respectively. (b) At 25 °C, multiple kink bands are observed and the enlarged views show fiber-matrix debonding. (e) At 100 °C, small amount of matrix plastic deformation and inter-fiber cracks are observed. (g) At −100 °C, the fracture surface is featured with rows of cusp. Scale bars: 500 μm. (For interpretation of the references to colour in this figure legend, the reader is referred to the web version of this article.)

greater energy absorption (Fig. 6(c)). For instance, the energy absorption increases 230% when the temperature decreases from 25 °C to −100 °C.

To understand this toughening mechanism, snapshots are taken at 1 ms, 2 ms, 2.5 ms and 3.5 ms after impact (Fig. 7), corresponding to the histories shown in Fig. 6(a) and (b). It is noticeable that the time needed for the specimen to break increases at lower temperatures with $v_{ini} = 5$ m/s, which is consistent with the displacement history in Fig. 6(a). Also note that the damage modes in the dynamic bending tests are similar to those in the static bending tests. The failures of the specimens at 25 °C and −20 °C are similar, damaged with a primary crack perpendicular to the fibers in the middle section. By contrast, the damage of the specimens at −60 °C expands to a larger region, and the specimen breaks into several pieces with delamination. Similarly, the damage of the specimen at −100 °C is fully delocalized, and a lot of parallel cracks are observed with extensive inter-fiber cracking over the entire specimen.

To further investigate the effect of the strain rate, impacts with $v_{ini} = 3$–10 m/s are carried out at room temperature. The energy absorption versus impact velocity is plotted in Fig. 6(d), where the dispersed data points indicates the intrinsic brittle behavior of the CFRP at room temperature. With a linear fitting, a slight improvement in the energy absorption at increased strain rate is revealed (at $\dot{\varepsilon} < 30\ s^{-1}$), which agrees well with the published results [24]. However, a stronger rate dependency might be expected at higher strain rates ($\dot{\varepsilon} > 50\ s^{-1}$) [33,34]. Besides, the critical penetration velocity at room temperature is found to be 3.4 m/s, bellowing which samples do not break. Furthermore, insights of the strain rate effect can also be given by comparing the static and dynamic testing results. Fig. 8 clearly shows that the energy absorption and maximum deflection are greater under dynamic loadings. More interestingly, the dynamic testing curves exhibit similar trend to the static testing curves, which would overlap with the static testing curves after applying a proper temperature shift. This similarity is known as the time-temperature equivalence of polymer

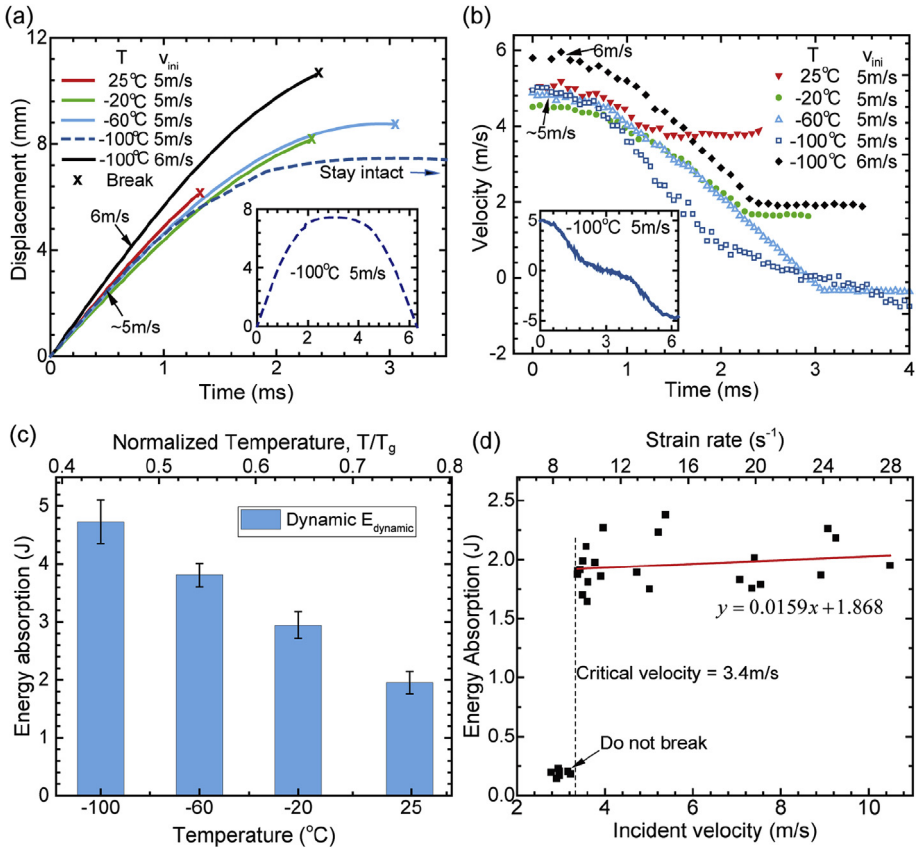

Fig. 6. Dynamic three-point bending results. (a) Displacement history, (b) velocity history, and (c) energy absorption at 25 °C, −20 °C, −60 °C and −100 °C. Insets in (a) (b) show the whole contact history at v_{ini} = 5 m/s, $T = -100$ °C. The histories of v_{ini} = 6 m/s, $T = -100$ °C are also plotted for comparison. (d) The energy absorption at room temperature (25 °C) with different incident velocities. A linear fit shows increasing of energy absorption with incident velocity.

materials [35], which arises from the viscoelastic nature of polymers that a shorter period of time and a colder temperature lead to similar effects of the polymer chain rearrangement (e.g. under tension/compression) [36]. In our experiments, the modulus of the polymer matrix is well controlled by this similarity [35], which further affects the macroscopic mechanical behavior of the composites. Therefore, similar trend is also found for the macroscopic mechanical behavior of the CFRP composites with respect to time and temperature. Moreover, this similarity is also known as "time-temperature superposition" principle which means that the effect of temperature and strain rate can be calculated separately and added together, suggesting a weak coupling between strain rate and temperature. However, when the strain rate is so high that the adiabatic heating developed under dynamic loading leads to drastic increase of temperature in the composite, which may trigger a change of polymer from the glassy to the rubbery state, the coupling between temperature and strain rate is intrinsically strong, and a more intricate model [37] should be used to analyze the coupling effect, which is out of the scope of this study.

4. Discussion

The temperature affects the mechanical response of CFRP composites mainly by 1) changing the mechanical properties of the polymer matrix, and 2) generating thermal stress that facilitates the formation of microcracks, which are the two fundamental factors in disscussing the micromechanical failure modes, toughenging mechanisms, thermal stress, and post break strength.

4.1. Micromechanical failure modes

The damage of a bending CFRP specimen usually initiates from the upper compressed surface, where microbuckling, kinking, and fiber failure could take place. The micromechanical compressive failure theories of these modes have been well studied and reported [31,38,39]. Microbuckling results from the alternating column structure of soft and hard material, which tends to evolve into the mode with lowest energy. There are two modes of microbuckling, namely the extension mode and the shear mode [39]. For fiber volume fraction greater than 20%, shear mode dominates (Fig. 4(b)). By contrast, kinking [31,40] is known as a catastrophic failure triggered by a sudden event in a local region, such as localized fiber fracture, fiber buckling, or matrix shear, leading to a sudden redistribution of the loads and excessive deformation of the surrounding matrix (Fig. 4(c)). Moreover, fiber failure takes place simply when the stress level reaches the compressive strength of the fiber (Fig. 4(d) and (e)). The critical stresses of the shear mode microbuckling σ_{1c}^{sh}, kinking σ_{1c}^{kink}, and fiber failure σ_{1c}^{fiber} in the fiber direction (1 direction) are calculated as [38]:

$$\sigma_{1c}^{sh} \cong k\frac{G_m}{1-V_f}, \tag{4}$$

$$\sigma_{1c}^{kink} \cong \frac{\tau_{m,fail}}{\theta_i + \gamma}, \tag{5}$$

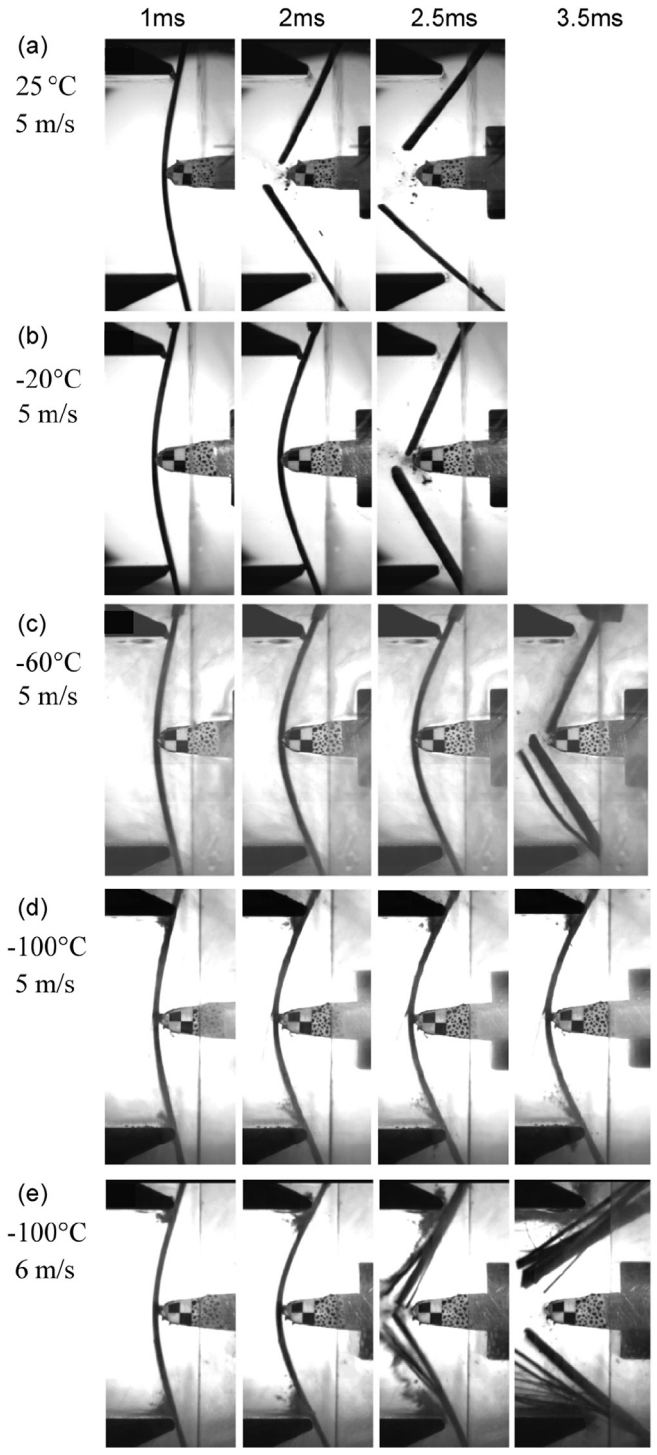

Fig. 7. Deformation images of the CFRP during dynamic bending tests at the temperature of (a) 25 °C, (b) −20 °C, (c) −60 °C, (d) and (e) −100 °C corresponding to the displacement and velocity histories in Fig. 6(a–b). The impact velocity is 5 m/s for (a–d) and 6 m/s for (e). Snapshots are captured at 1 ms, 2 ms, 2.5 ms and 3.5 ms after impact. At (a) 25 °C and (b) −20 °C specimens fail with one primary crack in the middle. At (c) −60 °C specimen breaks into several pieces. At −100 °C, the specimen stays intact with (d) $v_{ini} = 5$ m/s, and the damage expands to the entire specimen with extensive inter-fiber cracking with (e) $v_{ini} = 6$ m/s.

$$\sigma_{1c}^{fiber} \cong \sigma_{1c}^{F}\left[V_f + \left(1 - V_f\right)E_m \big/ E_f\right], \tag{6}$$

where G_m is the shear modulus of the matrix, E_m and E_f are the Young's modulus of the matrix and the fiber respectively, V_f is the volume fraction of the fiber, $k \approx 0.25$ is the knock down factor due to imperfections, $\tau_{m,fail}$ is the shear failure stress of the matrix, θ_i (in radian) is the initial fiber misalignment angle, γ is the shear strain at failure, and σ_{1c}^{F} is the ultimate compressive strength of the fiber.

Both σ_{1c}^{sh} and σ_{1c}^{kink} are highly dependent on the polymer properties. When the matrix becomes stiffer, σ_{1c}^{sh} tend to have a larger value than σ_{1c}^{kink} [31,41], leading to the failure mode transition from microbuckling to kinking as decreasing the temperature. This is verified by our results at 60 °C and 25 °C. Moreover, the temperature-dependence of the polymer modulus in the glassy regime can be approximated by linear equation $E_m = E_{m0}(1 - \alpha_m T/T_g)$ [36], a fitted equation for vinyl ester is $E_m = 3.9(1 - 0.5T/T_g)$ GPa. With the assumption of 5° fiber misalignment angle and use the data provided in Table 1, the failure modes at 60 °C, 25 °C, and −20 °C are found to be microbuckling, kinking and fiber failure, respectively. The corresponding critical stresses are estimated as: $\sigma_{1c,60°C}^{sh} \approx 504MPa$, $\sigma_{1c,25°C}^{kink} \approx 666MPa$ and $\sigma_{1c,-20°C}^{fiber} \approx 1018MPa$. These values clearly show the strengthening of the composite due to failure mode transition. Note that these values are around half of the flexural strength calculated from the experiments (Fig. 3(c)), because the normal stress is distributed linearly under bending.

At −100 °C, the specimens fail with fiber tensile break, and the tensile strength can be described by the rule of mixture [42], assuming that the ultimate tensile strain of the fiber is lower than that of the matrix ($\varepsilon_{mt}^{u} > \varepsilon_{ft}^{u}$),

$$\sigma_{1t}^{C} \cong \sigma_{1t}^{F}\left[V_f + \left(1 - V_f\right)\frac{E_m}{E_f}\right], \tag{7}$$

where σ_{1t}^{C}, σ_{1t}^{F} are the ultimate tensile strength of the composite and the fiber respectively. When $E_f >> E_m$, Eqn. (7) is simplified as $\sigma_{1t}^{C} \cong V_f \sigma_{ft}^{F}$, suggesting that ultimate tensile strength of the composite σ_{1t}^{C} is relatively insensitive to the matrix properties.

It is clear from Eqns. (4)–(6) to see that the critical failure stress of compression increases as decreasing the temperature, due to the increasing of the matrix stiffness and the yield strength. By contrast, the failure stress of tension is insensitive to the temperature change. At 25 °C, 60 °C, and 100 °C, the top surface compressive strength is lower than the bottom surface tensile strength [42], thus the failure initiates from the top surface (in Fig. 4(a–c)). As temperature decreases, the compression failure stress increases, and at temperatures −20 °C and −60 °C, the failure stress of compression is close to that of tension. Therefore, the upper region and bottom region of the specimens fail simultaneously, characterized by one crack penetrate through the whole specimen. When the temperature further decreases, the critical stress of microbuckling and kinking is higher than the tensile strength, and the failure mode of the CFRP transfers from upper region compressive failure to bottom region fiber breakage failure, verified by the bottom fibers breakage observed at −100 °C (Fig. 4(f)). This transition of failure mode plays a key role in improving the strength and the toughness of the CFRP composites at low temperatures.

4.2. Toughing mechanisms

An intuitive explanation of the observed low temperature toughing is shown Fig. 9(a–b), where the temperature dependent

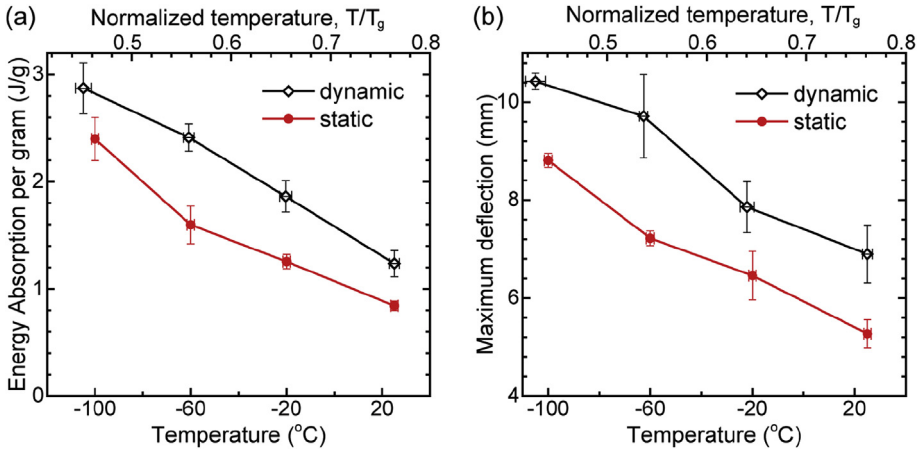

Fig. 8. Comparison between static and dynamic three-point bending results (v_{ini} = 5 m/s): (a) energy absorption per gram, (b) maximum deflection at break.

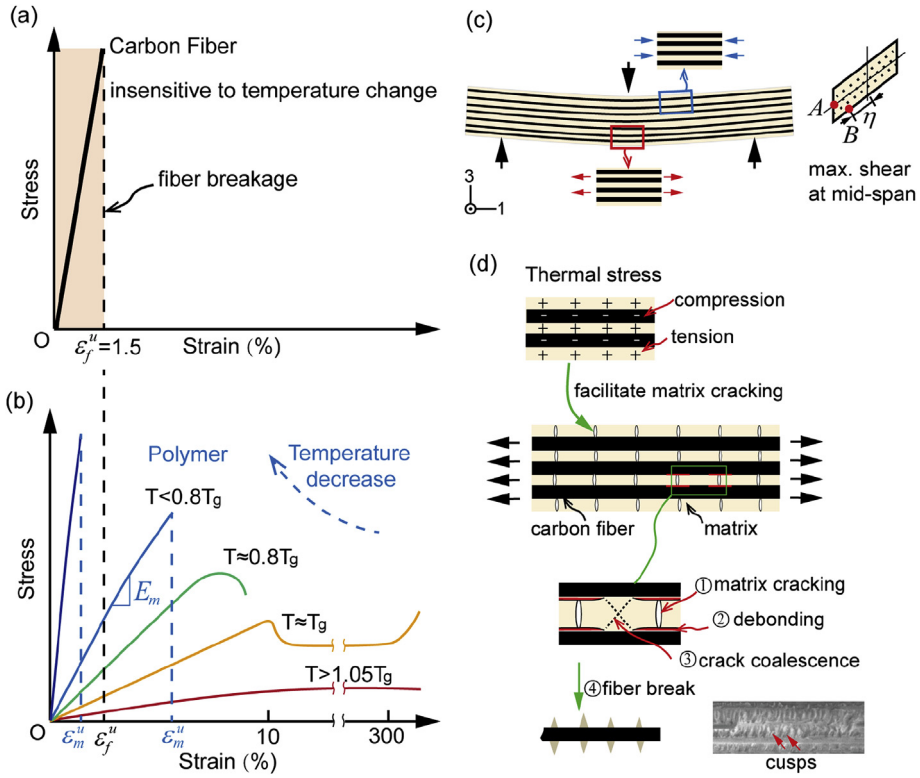

Fig. 9. Temperature effect on CFRP composites. The tensile response of (a) the carbon fiber and (b) the polymer matrix at different temperatures. Polymer becomes stiffer and more brittle at lower temperatures, while the mechanical response of the carbon fiber is insensitive to the temperature. (c) Under 3-point bending load, the upper/bottom region is in compression/tension, the maximum shear stress of a wide rectangle beam is at point A (maximum τ_{13}) and point B (maximum τ_{12}). (d) The cracking process predicted by a shear lag model when $\varepsilon_m^u < \varepsilon_f^u$, the broken fiber surfaces show rows of cusps. Thermal stress developed at the decreased temperature facilitates the matrix cracking, "+" represents tension and "-" represents compression.

tensile stress-strain curve of the carbon fiber and the polymer matrix are shown (similar figure exists for compression). Take tensile failure as an example, when the ultimate failure strain of the matrix is larger than that of the fiber ($\varepsilon_m^u > \varepsilon_f^u$), which is true in most CFRP composites, the only material constant of the matrix comes into the composite failure model is its modulus E_m, which increases considerably as decreasing the temperature. By contrast, the brittleness of the polymer at frigid temperatures is related to ε_m^u, which is excluded from damage model when $\varepsilon_m^u > \varepsilon_f^u$. Similar conclusions can be made in the compressed region.

Furthermore, when temperature is further decreased, the failure strain of the matrix would be smaller than that of the fiber $\varepsilon_m^u < \varepsilon_f^u$, which leads to a more complex damage process. Such a case has been studied in Refs. [36,37]. The damage initiates with multiple matrix cracks, which are then accompanied or followed sequentially by fiber/matrix debonding, crack coalescence, and fiber breakage. A typical failure progression [43] is shown in Fig. 9(d). The initialization of the transverse matrix cracks is facilitated by the thermal stress, and rows of cusps are formed on the fiber surfaces after the breakage of the fibers. Such cusps are found in the post-

mortem specimens at −100 °C in Fig. 5(g–h). Importantly, the crack path with cusps is capable to dissipate more energy than a smooth crack because of a longer crack path.

Extensive secondary inter-fiber cracking at −60 °C and −100 °C (Fig. 4(e–f)) also contributes to a greater energy absorption. These secondary cracks initiate when interfacial shear stress τ_i is larger than the interfacial shear strength F_{is} [44]. For a wide rectangular cantilever beam [45] ($b >> d$), the shear stress generated by external bending has a maximum τ_{13} at point A and a maximum τ_{12} at point B as shown in Fig. 9(c). These maximum shear stresses are calculated as $\tau_{13,A} = 4.58P/bd$ and $\tau_{12,B} = 3.54P/bd$ with $\eta = 0.41b$. As a result, inter-fiber cracks tend to be gathered at these locations, which is consistent with our observation.

As a summery, "a stiffer matrix makes composites tougher" is the basic mechanism of low temperature toughening. But this does not depict the whole picture, since the cusped crack surface and delocalized cracking also contribute to the toughening. More importantly, at lower temperatures, the matrix becomes stiffer but has a smaller failure strain, which is analogy to the general stiffness-toughness inversion relation of materials. This remarkable feature is highly related to the fiber reinforced geometry of the composite. When adopting this idea to CFRP applications at room temperature, it's possible to choose stiffer but less ductile polymers to improve the toughness of the CFRP composites.

4.3. Effect of thermal stress

When the external force and the temperature change act simultaneously, the resultant local nominal strain is calculated by adding the internal stress contribution and the temperature contribution as $\varepsilon = \varepsilon_S + \varepsilon_T$ [46], where the free thermal expansion part is given by $\varepsilon_T = \alpha \Delta T$. In unidirectional CFPR, thermal stress is mainly developed in the fiber direction where the thermal deformation mismatch between the matrix and the fiber is largest. Assume free boundary condition of the specimen and from the stress equilibrium between the fiber and the matrix, the strain of the matrix produced by internal force at a temperature drop ΔT [46] is derived as:

$$\varepsilon_{S,m} = \frac{V_f E_f \left(\alpha_m - \alpha_f\right)}{V_f E_f + \left(1 - V_f\right) E_m} \Delta T, \tag{8}$$

and the strain in the fiber produced by the internal force is,

$$\varepsilon_{S,f} = \frac{\left(1 - V_f\right) E_m \left(\alpha_f - \alpha_m\right)}{V_f E_f + \left(1 - V_f\right) E_m} \Delta T, \tag{9}$$

where α_m and α_f are the coefficients of thermal expansion for the matrix and the fiber, respectively. When $E_f >> E_m$, Eq. (8) and Eq. (9) gives $\varepsilon_{S,m} \approx (\alpha_m - \alpha_f)\Delta T$, and $\varepsilon_{S,f} \to 0$. For the CFRP composite with $V_f = 0.5$,

$$\sigma_m = -\sigma_f \approx E_m \left(\alpha_m - \alpha_f\right) \Delta T. \tag{10}$$

For example, when temperature drops from 30 °C (typical cure temperature of vinyl ester) to −100 °C, the thermal strain of the matrix is estimated to be $\varepsilon_{S,m} \approx 0.3\%$. This is 5–10% of the matrix ultimate failure strain at room temperature ($\varepsilon_m^u = 4 \sim 6\%$), and could be a more significant portion of its ultimate failure strain at −100 °C.

Moreover, because of the thermal stress, the matrix is initially in tension ($\sigma_m > 0$) and the fibers are initially in compression ($\sigma_f < 0$). When the specimen is further loaded with three-point bending, the total stress is the addition of the thermal stress and the bending contributed stress $\sigma = \sigma_T + \sigma_B$. Therefore, thermal stress accelerates the fiber compression failure, facilitates the matrix tensile cracking, but delays the fiber tensile failure.

4.4. Post break strength

As observed in the static bending tests, damages at 60 °C, 100 °C and −100 °C show post break strength, in contrast to the catastrophic damage at intermediate temperatures (−60 °C, −20 °C). The post break strength is associated with: 1) the difference between the critical failure stress of the top compressive layer and the bottom tensile layer. A larger difference means a larger post break energy absorption ability. For example, the stored strain energy is released when the top layer kinking is triggered at 25 °C. If the bottom layer has enough capability to arrest the energy, the crack is successfully captured, and the specimen will show post break strength. 2) A micromechanical shear-lag and fiber pull out mechanism at −100 °C temperature. At extremely low temperature, the ultimate tensile failure strain of the matrix is small (also undermined by the thermal strain $\varepsilon_{S,m}$), the damage in the matrix initiates before that in the fibers. As a result, numerous microcracks perpendicular to the fiber direction are formed in the matrix [42] (Fig. 9(d)), the resultant structure is similar to the "brick and mortar" structure of nacre [47,48]. This "brick and mortar" structure is reported for its good energy absorption and crack delocalization abilities [49]. One can notice that in Fig. 3(a), the post break strength at −100 °C is more stable as compared to the decreasing post break strength at 60 °C. The unbroken part of the specimen (Fig. 4(f)), together with the delocalized damage, the fiber pulling-out (Fig. 5(h)), and the fracture surface profile of cusps [32] (Fig. 5(g)), strongly supports these mechanisms.

5. Conclusion

In summary, we have used static and dynamic three-point bending tests to investigate the mechanical response and failure process of the unidirectional CFRP composites at various temperatures. Our results indicate that unidirectional CFRP composites become stronger and tougher at lower temperatures (−100 °C–100 °C) under three-point bending load. In particular, we have presented a theoretical analysis of the temperature dependent mechanical behaviors of CFRP composites based on post-mortem photographs, and revealed the underlying toughening mechanisms as 1) improved critical stress of microbuckling, kinking, and ultimate tensile stress at lower temperatures, 2) a failure mode transition from upper layer microbuckling to bottom layer tensile breakage, and 3) formation of extensive microcracks when the temperature is extremely low. These mechanisms come from the "brittle" nature of the polymer matrix at lower temperatures – higher Young's modulus and smaller ultimate tensile strain. Moreover, compared to the effect of the matrix properties change, the effect of the thermal stress is secondary. The effect of increasing strain rate is found similar to that of temperature decreasing, which improves the mechanical properties of the CFRP composites. Importantly, the finding reported here offers pathways to improve the structure integrity design by taking advantage of the favorable damage patterns and avoiding the unfavorable ones.

Acknowlegdgemnets

The authors gratefully acknowledge the support from the Office of Naval Research (Dr. Yapa Rajapakse, Solid Mechanics Program)

and the National Science Foundation. Z. Jia thanks Xuedong Zhai (Purdue University) for his assistance in setting up the SHPB apparatus. The authors thank Joseph Nguyen and Nicholas Genovese for their assistance in mechanical testing, and Dr. Shuyu Wang for his assistance in SEM observation. The authors also acknowledge the use of the Center for Functional Nanomaterials facility at Brookhaven National Laboratory.

References

[1] C. Soutis, Carbon fiber reinforced plastics in aircraft construction, Mater. Sci. Eng. A 412 (1) (2005) 171–176.
[2] K. Friedrich, A.A. Almajid, Manufacturing aspects of advanced polymer composites for automotive applications, Appl. Compos. Mater. 20 (2) (2013) 107–128.
[3] R.M. Jones, Mechanics of Composite Materials, CRC press, 1998.
[4] M.F. Ashby, Materials Selection in Mechanical Design, Butterworth-Heinemann Press, 2005.
[5] P. Kim, A comparative study of the mechanical performance and cost of metal, FRP, and hybrid beams, Appl. Compos. Mater. 5 (3) (1998) 175–187.
[6] A. Manalo, T. Aravinthan, A. Fam, B. Benmokrane, State-of-the-art review on FRP sandwich systems for lightweight civil infrastructure, J. Compos. Constr. (2016) 04016068.
[7] J.W. Chin, T. Nguyen, K. Aouadi, Effects of environmental exposure on fiber-reinforced plastic (FRP) materials used in construction, J. Compos. Technol. Res. 19 (4) (1997) 205–213.
[8] A. Afshar, M. Alkhader, C.S. Korach, F.-P. Chiang, Effect of long-term exposure to marine environments on the flexural properties of carbon fiber vinylester composites, Compos. Struct. 126 (2015) 72–77.
[9] T. Nakamura, R. Singh, P. Vaddadi, Effects of environmental degradation on flexural failure strength of fiber reinforced composites, Exp. Mech. 46 (2) (2006) 257–268.
[10] A.K. Kaw, Mechanics of Composite Materials, CRC press, 2005.
[11] C. Mahieux, K. Reifsnider, Property modeling across transition temperatures in polymers: a robust stiffness–temperature model, Polymer 42 (7) (2001) 3281–3291.
[12] R. Reed, M. Golda, Cryogenic properties of unidirectional composites, Cryogenics 34 (11) (1994) 909–928.
[13] S. Sánchez-Sáez, T. Gómez-del Rıo, E. Barbero, R. Zaera, C. Navarro, Static behavior of CFRPs at low temperatures, Compos. Part B Eng. 33 (5) (2002) 383–390.
[14] M. Garrido, J.R. Correia, T. Keller, Effects of elevated temperature on the shear response of PET and PUR foams used in composite sandwich panels, Constr. Build. Mater. 76 (2015) 150–157.
[15] S. Feih, Z. Mathys, A. Gibson, A. Mouritz, Modelling the tension and compression strengths of polymer laminates in fire, Compos. Sci. Technol. 67 (3) (2007) 551–564.
[16] A. Gibson, Y.-S. Wu, J. Evans, A. Mouritz, Laminate theory analysis of composites under load in fire, J. Compos. Mater. 40 (7) (2006) 639–658.
[17] J. Smith, The vertical temperature distribution and the layer of minimum temperature, J. Appl. Meteorol. 2 (5) (1963) 655–667.
[18] V. Agrawal, Satellite Technology: Principles and Applications, John Wiley & Sons, 2011.
[19] D.J. Mildrexler, M. Zhao, S.W. Running, Satellite finds highest land skin temperatures on Earth, Bull. Am. Meteorol. Soc. (2011) 855.
[20] J. Turner, P. Anderson, T. Lachlan-Cope, S. Colwell, T. Phillips, A. Kirchgaessner, G.J. Marshall, J.C. King, T. Bracegirdle, D.G. Vaughan, Record low surface air temperature at Vostok station, Antarctica, J. Geophys. Res. Atmos. 114 (D24) (2009).
[21] J. Garratt, Extreme maximum land surface temperatures, J. Appl. Meteorol. 31 (9) (1992) 1096–1105.
[22] J. Schutz, Properties of composite materials for cryogenic applications, Cryogenics 38 (1) (1998) 3–12.
[23] J. López-Puente, R. Zaera, C. Navarro, The effect of low temperatures on the intermediate and high velocity impact response of CFRPs, Compos. Part B Eng. 33 (8) (2002) 559–566.
[24] Y. Ou, D. Zhu, H. Zhang, Y. Yao, B. Mobasher, L. Huang, Mechanical properties and failure characteristics of CFRP under intermediate strain rates and varying temperatures, Compos. Part B Eng. 95 (2016) 123–136.
[25] G. Hartwig, Overview of advanced fibre composites, Cryogenics 28 (4) (1988) 216–219.
[26] A. Standard, D638, 2010, Standard Test Method for Tensile Properties of Plastics, ASTM International, West Conshohocken, PA, 2010, https://doi.org/10.1520/D0638-10.
[27] J. Hu, G. Lu, H. Yang, T. Yu, J. Xu, Dynamic response of internally nested hemispherical shell system to impact loading, Thin-Walled Struct. 120 (2017) 29–37.
[28] D. Hu, K. Meng, H. Jiang, J. Xu, R. Liu, Strain rate dependent constitutive behavior investigation of AerMet 100 steel, Mater. Des. 87 (2015) 759–772.
[29] M. Stone, B. Fink, T. Bogetti, J. Gillespie, Thermo-chemical response of vinylester resin, Polym. Eng. Sci. 40 (12) (2000) 2489–2497.
[30] S. Pinho, L. Iannucci, P. Robinson, Physically-based failure models and criteria for laminated fibre-reinforced composites with emphasis on fibre kinking: Part I: Development, Compos. Part A Appl. Sci. Manuf. 37 (1) (2006) 63–73.
[31] C.R. Schultheisz, A.M. Waas, Compressive failure of composites, part I: testing and micromechanical theories, Prog. Aerosp. Sci. 32 (1) (1996) 1–42.
[32] K. Pannkoke, H.-J. Wagner, Fatigue properties of unidirectional carbon fibre composites at cryogenic temperatures, Cryogenics 31 (4) (1991) 248–251.
[33] H. Al-Zubaidy, X.-L. Zhao, R. Al-Mahaidi, Mechanical characterisation of the dynamic tensile properties of CFRP sheet and adhesive at medium strain rates, Compos. Struct. 96 (2013) 153–164.
[34] A. Gilat, R.K. Goldberg, G.D. Roberts, Experimental study of strain-rate-dependent behavior of carbon/epoxy composite, Compos. Sci. Technol. 62 (10) (2002) 1469–1476.
[35] S. Lyu, J. Schley, B. Loy, D. Lind, C. Hobot, R. Sparer, D. Untereker, Kinetics and time– temperature equivalence of polymer degradation, Biomacromolecules 8 (7) (2007) 2301–2310.
[36] L.J. Gibson, M.F. Ashby, Cellular Solids: Structure and Properties, Cambridge university press, 1999.
[37] J. Richeton, S. Ahzi, K. Vecchio, F. Jiang, A. Makradi, Modeling and validation of the large deformation inelastic response of amorphous polymers over a wide range of temperatures and strain rates, Int. J. Solids Struct. 44 (24) (2007) 7938–7954.
[38] P. Jelf, N. Fleck, Compression failure mechanisms in unidirectional composites, J. Compos. Mater. 26 (18) (1992) 2706–2726.
[39] B.W. Rosen, Mechanics of Composite Strengthening, 1965.
[40] B. Budiansky, Micromechanics, Comput. Struct. 16 (1) (1983) 3–12.
[41] R. Gutkin, S. Pinho, P. Robinson, P. Curtis, On the transition from shear-driven fibre compressive failure to fibre kinking in notched CFRP laminates under longitudinal compression, Compos. Sci. Technol. 70 (8) (2010) 1223–1231.
[42] I.M. Daniel, O. Ishai, I.M. Daniel, I. Daniel, Engineering Mechanics of Composite Materials, Oxford university press, New York, 1994.
[43] I. Daniel, Characterization of Deformation and Damage in Brittle Matrix Composite Materials, DTIC Document, 1996.
[44] T.-W. Chou, Microstructural Design of Fiber Composites, Cambridge University Press, 2005.
[45] S.P. Timoshenko, J. Goodier, Theory of Elasticity, 2011.
[46] M.R. Eslami, R.B. Hetnarski, J. Ignaczak, N. Noda, N. Sumi, Y. Tanigawa, Theory of Elasticity and Thermal Stresses, Springer, 2013.
[47] A. Jackson, J. Vincent, R. Turner, The mechanical design of nacre, Proc. R. Soc. Lond. B Biol. Sci. 234 (1277) (1988) 415–440.
[48] Y. Chen, L. Wang, Tunable band gaps in bio-inspired periodic composites with nacre-like microstructure, J. Appl. Phys. 116 (6) (2014) 063506.
[49] F. Barthelat, H. Tang, P. Zavattieri, C.-M. Li, H. Espinosa, On the mechanics of mother-of-pearl: a key feature in the material hierarchical structure, J. Mech. Phys. Solids 55 (2) (2007) 306–337.